Angewandte Chemie
Eine Zeitschrift der Gesellschaft Deutscher Chemiker

Supporting Information

Coordination Assembly of Discoid Nanoparticles**

Kenji Hirai, Bongjun Yeom, Shu-Hao Chang, Hang Chi, John F. Mansfield, Byeongdu Lee, Sungsik Lee, Ctirad Uher, and Nicholas A. Kotov**

ange_201502057_sm_miscellaneous_information.pdf

Supporting Information

Experimental Section

Coordination Assembly: FeS_2 NPs were synthesized according to a previously published procedure.[S1] 10 mL of an aqueous solution of $ZnCl_2$ (10 mM) was slowly added to 10 mL of an aqueous solution of FeS_2 NPs (12.0 g mL^{-1}, estimated by ICP). The precipitates were washed with water two times and harvested by centrifugation.

Hall Effect Measurements: Samples with typical dimensions of 2 mm (width) by 6 mm (length) were prepared for electronic properties measurements, where fine copper wires were attached to the samples (in Hall bar and/or four probe configuration) using DuPont CP4922N silver epoxy. The thickness of the sample and the probe separation were estimated using SEM. Measurements of the Hall coefficient R_H and electrical resistivity ρ were performed using Keithley 6221 DC current source and 2182A voltmeter, in the temperature range of 1.8 K to 400 K in a Quantum Design Magnetic Property Measurement System (MPMS), equipped with a 5.5 T superconducting magnet.

Electrochemical Measurements: Cyclic voltammetry (CV) was carried out with a BASi EC Epsilon apparatus utilizing the three-electrode configuration of an Au substrate electrode, a Pt auxiliary electrode and an Ag/AgCl reference electrode. The electrocatalytic reduction processes were studied in an acetonitrile solution of benzyl chloride (10 mmol L^{-1}) and tetraethylammonium tetrafluoroborate (50 mmol L^{-1}). The photocurrent response was investigated in acetonitrile containing tetraethylammonium tetrafluoroborate (0.2 mol L^{-1}) under –200 mV. The electrode was illuminated by the light source EXFO X-Cite, Series 120.

Substrate preparation: The substrates (gold, silicon and quartz) were cleaned in a piranha solution (H_2SO_4 : 30% H_2O_2 = 3 : 1). The cleaned substrates (silicon and quartz) were

immersed in a 1 vol% toluene solution of 10-undecenyltrichlorosilane for 1 day. After washing and drying, the vinyl group of the 10-undecenyltrichlorosilane was oxidized by immersing the substrates into an aqueous solution (20 mL) of 2 mg of $KMnO_4$ and 84 mg of $NaIO_4$.[S2] The thoroughly cleaned gold substrate was immersed in a 1 mmol L^{-1} solution (ethanol) of 11-mercaptoundecanoic acid.[S3]

Coordination assembly of macroscale films using layer-by-layer deposition: The NPs and metal ions were sequentially deposited by the following protocol: (1) dipping the substrate into the solution of $ZnCl_2$ (20 mM) for 10 min, (2) washing the substrate to remove chloride ions and extraneous zinc ions, (3) dipping the substrate into the solution of NPs (24.0 g mL^{-1}) for 10 min, (4) washing the substrates to remove extraneous NPs, (5) repeating processes (1)-(4).

Transmission Electron Microscopy (TEM): The aqueous solution containing NPs or sheets was cast on the TEM grid (Ultrathin Carbon Film on Holey Carbon Support Film, 400 mesh Copper, Ted Pella Inc.), and dried in air. The samples were observed by JEOL 3011 High Resolution TEM. The TEM tomography was carried out by JEOL 2100F Cs-corrected scanning TEM.

Scanning Electron Microscopy (SEM): The aqueous solution containing the sheets was casted on a silicon wafer and dried in air. The samples were coated by gold spattering and observed using a FEI Nova 200 Nanolab apparatus.

Atomic Force Microscopy (AFM): The aqueous solution containing NPs was casted on a silicon wafer. The samples were observed by Veeco Dimension Icon AFM. The silicon nitride probe of “ScanAsyst - Air (Bruker)” was utilized to scan the surface height of the sample.

X-ray diffraction (XRD): The XRD patterns were collected on a Rigaku Rotating Anode X-Ray Diffractometer. The diffractions were recorded in the range 2θ = 25-80°. The

diffractions were assigned to Miller indices (hkl) by JADE (Rigaku).

Fourier Transform Infrared Spectroscopy (FTIR): The NPs or sheets were cast on a gold substrate. The reflectance IR spectrum was collected on a Thermo Fischer Nicolet 6700 FT-IR spectrometer.

Small Angle X-ray Scattering (SAXS): SAXS data were collected at the beamline 12-ID-B at the Advanced Photon Source at the Argonne National Laboratory. 14keV X-ray beam was focused to a sample with a size of 300 x 20μm^2. Pilatus2M detector was used at about 1.8m downstream of the sample to measure scattering signals.

Extended X-ray Absorption Fine Structure (EXAFS): EXAFS measurements were performed at the 12 BM-B station of the Advanced Photon Source, Argonne National Laboratory. The powder samples and two reference sample (Zn stearate) was mounted between two Kapton tapes. The Extended X-ray absorption fine structure (EXAFS) spectra were recorded at the Zn K-edge (9,659 eV) in transmission mode at room temperature using two ion chambers. The energy was calibrated using a zinc foil. EXAFS data processing and fitting were performed with Athena and Artemis

Zeta Potential Measurements: The zeta potentials of all samples were measured on a Malvern Zetasizer Nano Range apparatus. The zeta potential of as-synthesized NPs dispersed in water (12.0 mg L^{-1}) was measured. As soon as the $ZnCl_2$ aqueous solution (10 mM) was mixed with the NP solution (12.0 mg L^{-1}), the zeta potential of NPs was measured.

Ultraviolet–visible (UV-vis) Spectroscopy: UV-vis spectra were collected on an Agilent 8453 spectrometer (Agilent Technologies).

Supporting Data

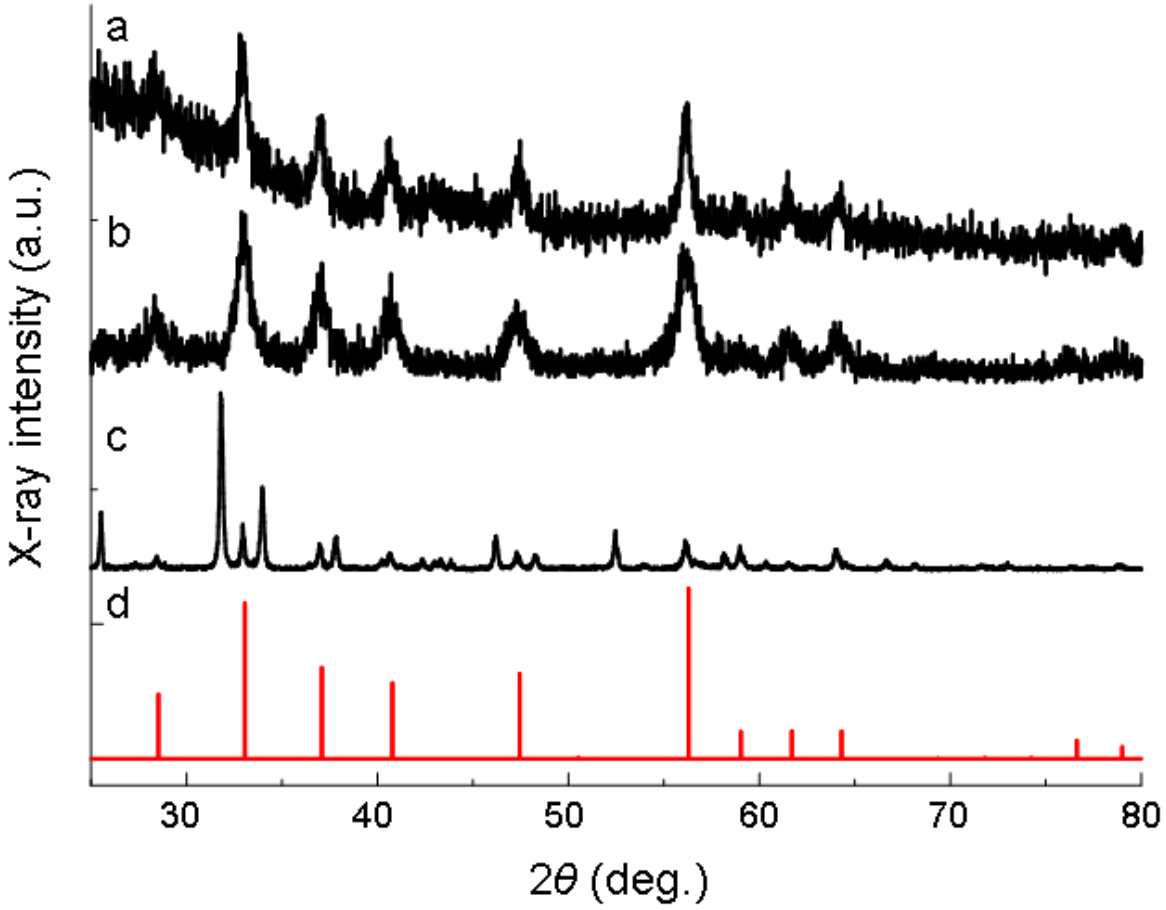

Figure S1. XRD patterns of (a) original FeS_2 NPs, (b) nanosheets formed by coordination of pyrite NPs with 10 mM of $ZnCl_2$ at 25 °C and pH 6, and (c) nanorods formed by coordination of pyrite NPs with 10 mM of $ZnCl_2$ at 70 °C and pH 6 shown in Figure S11c. (d) Simulated XRD patterns of pyrite FeS_2.

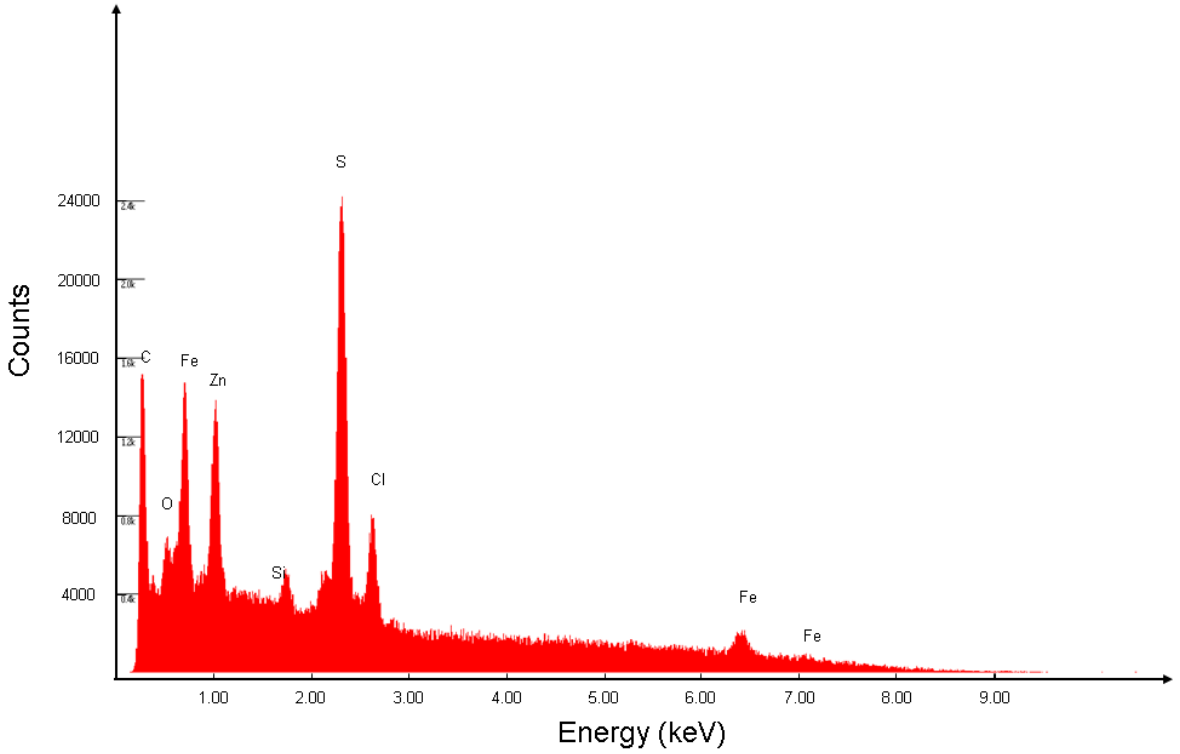

Figure S2. EDX spectrum of the nanosheets formed by coordination of pyrite NPs with 10 mM of $ZnCl_2$ at 25 °C and pH 6.

.

<u>Comment 1</u>: A certain amount of Cl^- was observed in the product because the residual reaction solution contained $ZnCl_2$. The Cl^- was not detected after subsequent washing, which suggested that the residual $ZnCl_2$ was completely removed (Fig. 3a).

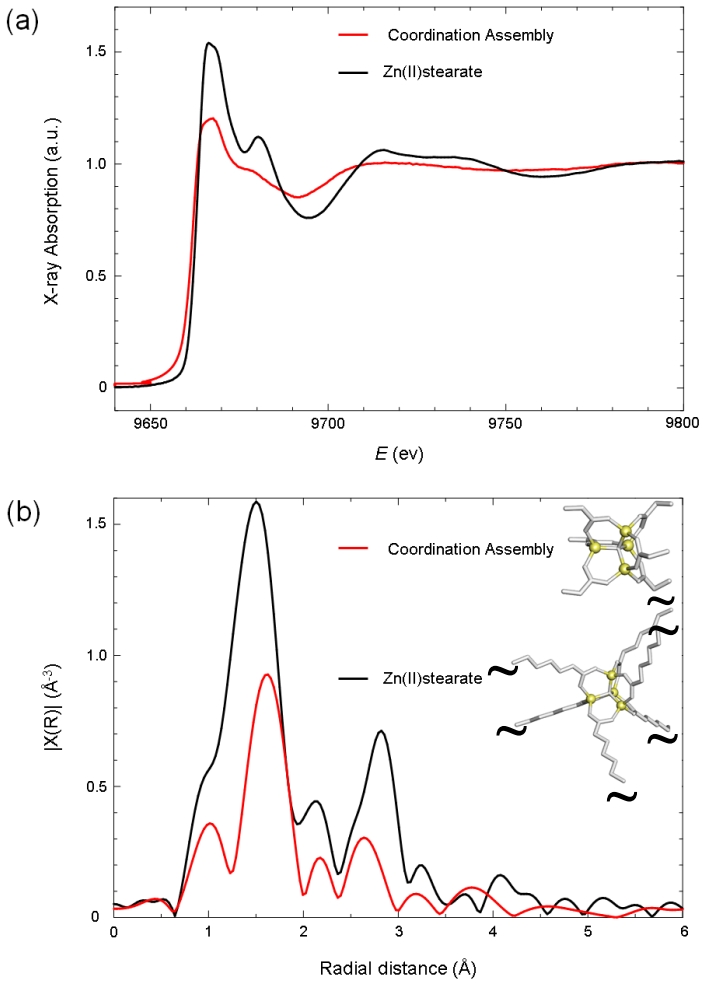

Figure S3. Synchrotron X-ray absorption fine structure spectroscopy (XAFS) of the nanosheets obtained by the coordination assembly of NPs with Zn^{2+} (red) and Zn(II) stearate ($[Zn_4(\mu_4\text{-}O)](C_{17}H_{34}COO^{-})_6$) (black). (a) XAFS plot, (b) Fourier-transformed spectra. The inset shows the coordination geometry of the $[Zn_4(\mu_4\text{-}O)]^{6+}$ cluster and six carboxylates. The aliphatic chains of the stearate units are truncated for clarity.

Comment 2: Fourier-transformed spectra for the nanosheets (red) and Zn(II) stearate are essentially similar, meaning that the coordination clusters in nanosheets have same coordination geometry with Zn(II)stearate, e.g. $[Zn_4(\mu_4\text{-}O)]^{6+}$. The coordination geometry of Zn(II) stearate has been discussed in multiple previous studies.[S4-S5] $[Zn_4(\mu_4\text{-}O)]^{6+}$ clusters are bridged by coordination bonds with six carboxylates of TGA.

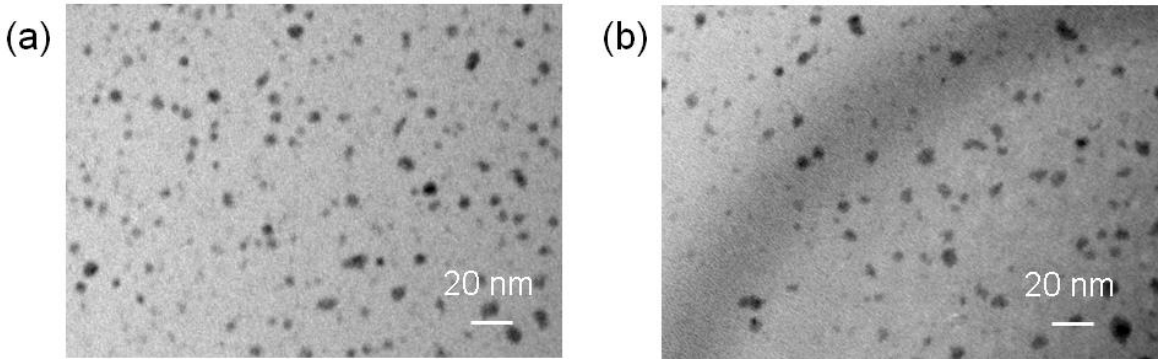

Figure S4. TEM images of (a) the original NPs and (b) NPs obtained by EDTA-induced disassembly of the previously formed nanosheets.

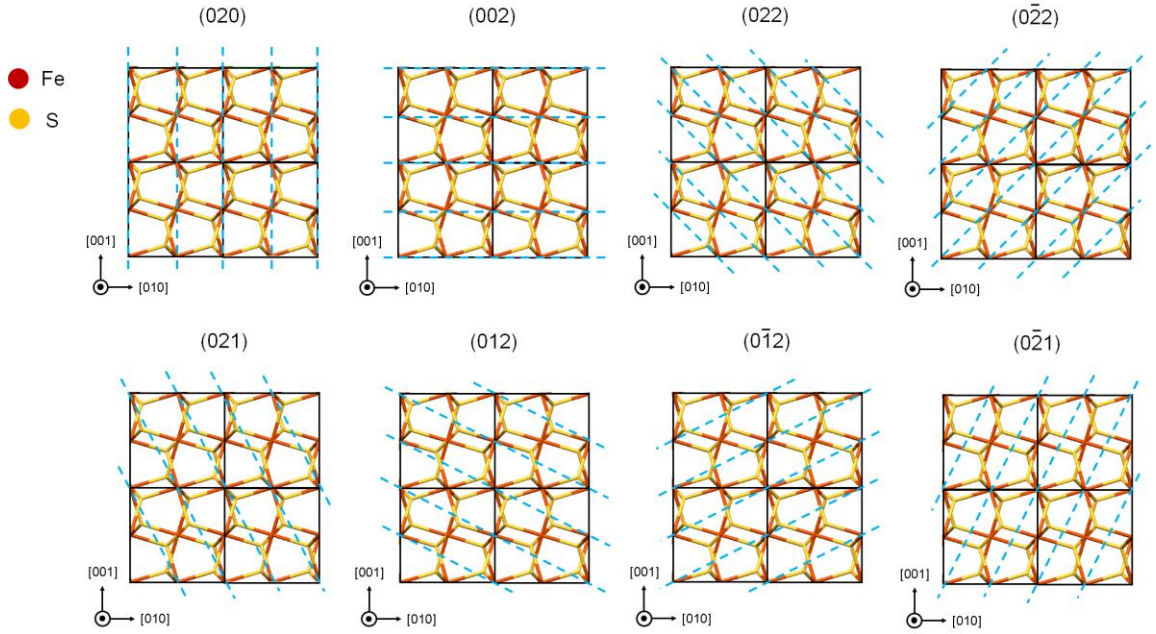

Figure S5. The diffraction schematics of FeS_2 discoids with *a* axis orientation. The black box indicates a unit cell of FeS_2. The blue dotted lines indicate the diffraction planes.

Comment 3: When the *a* axis is oriented along the surface normal, the following diffractions can be observed, 002, 020, 022, 0-22, 021, 012, 0-12 and 0-21. Since the crystal symmetry of FeS_2 pyrite is cubic (space group: *Pa3*), *a*, *b* and *c* axes are crystallographically equivalent. The d-spacing of 200, 020 and 002 are all equal (d = 2.71 Å). The d-spacing of 021, 012 and 0-12 are all equal (d = 2.21 Å). The d-spacing of 220, 022 and 02-2 are all equal (d = 1.94 Å). Therefore, the electron diffractions of FeS_2 discoids with *a* axis orientation give only three diffraction spots corresponding to d-spacings for 200, 210 and 220.

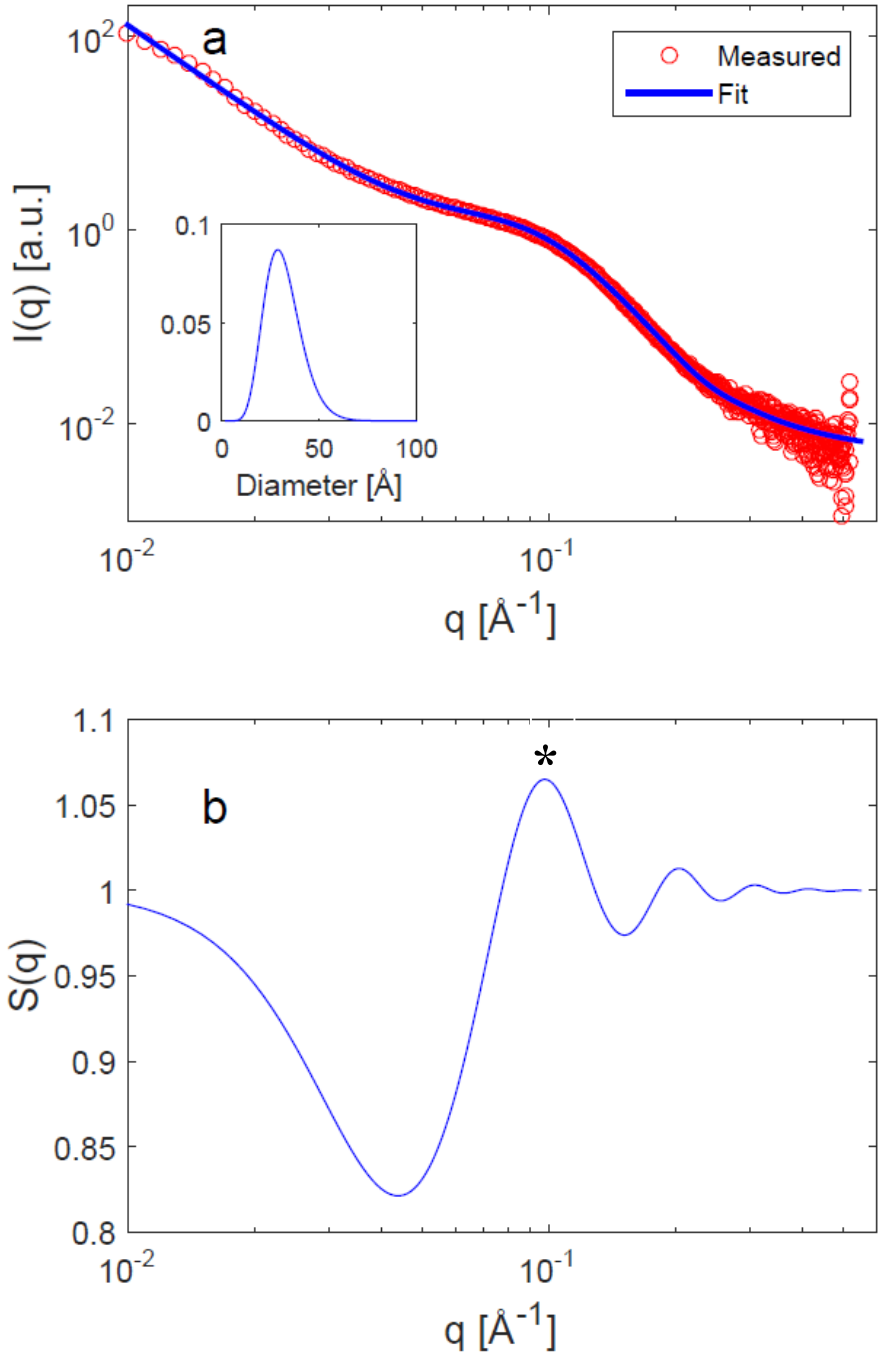

Figure S6. Synchrotron small angle X-ray scattering (SAXS) of the nanosheets obtained by the coordination assembly of NPs with Zn^{2+}. a) Measured intensity (symbol) and model fit (line). Inset is the size distribution of discoid diameter. b) The structure factor obtained from the fit in a. The star marks the position of the SAXS peak maximum.

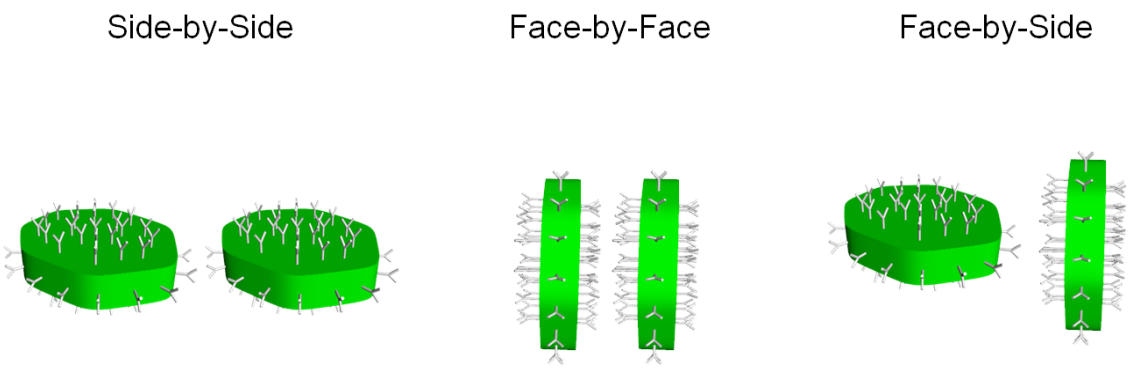

Figure S7. Possible orientations of two discoid NPs in the assemblies.

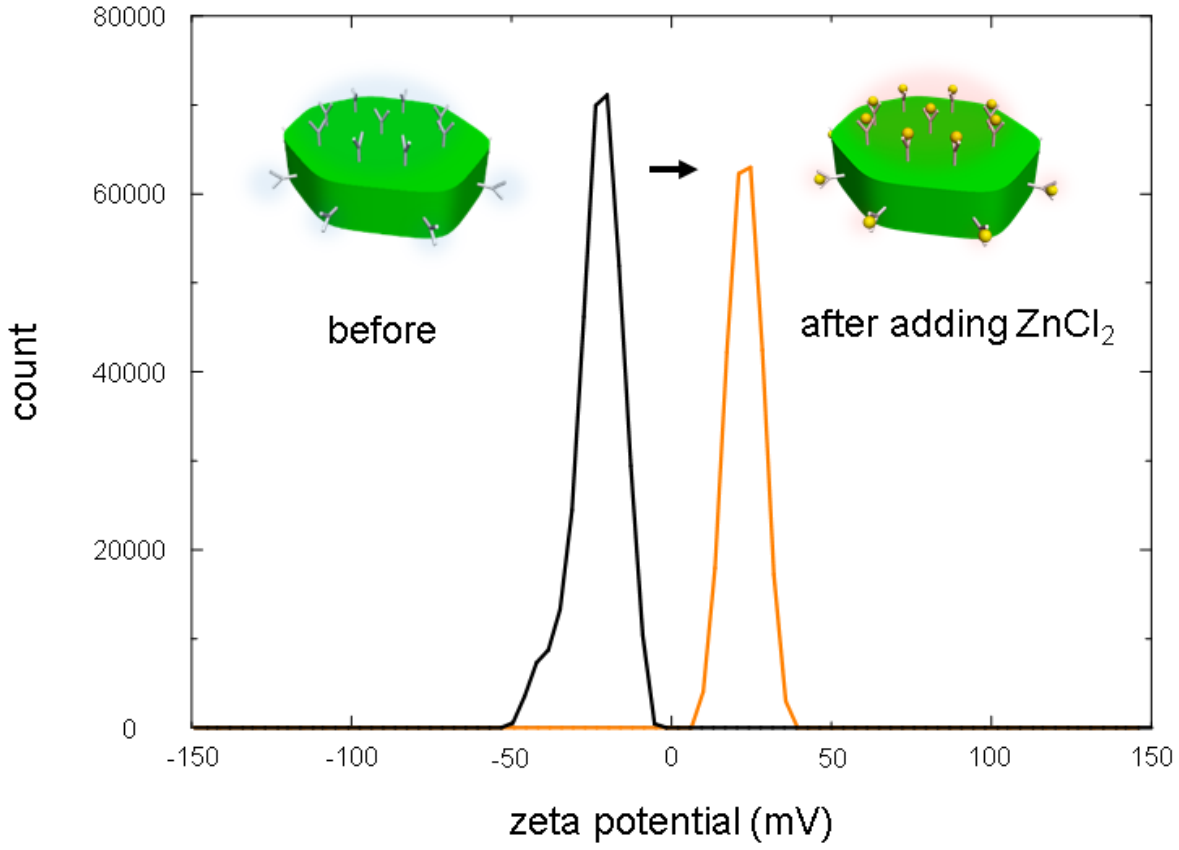

Figure S8. Zeta potential of FeS_2 NPs before (black) and after mixing with 10 mmol L^{-1} $ZnCl_2$ solution (orange).

Comment 4: As an example of media effects, we found that the well-defined sheets formed only for $5 \leq pH \leq 6$ (Fig. S9). This pH range can be compared to the pK_a of 3.67 for carboxylate groups in free TGA; pKa values of mercaptoacids, such as TGA, are known to increase when attached to NP surfaces.[S6] No precipitate was formed for $pH \leq 4$ due to protonation of TGA surface ligands. Oblong NP assemblies ~250 nm in length were formed for $7 \leq pH \leq 9$ transitioning to smaller ~50 nm agglomerates because of the increasing deprotonation of TGA and instability of $[Zn_4(\mu_4\text{-}O)]^{6+}$ at high pH.

Replacement of $ZnCl_2$ with NaCl or $CaCl_2$ at the tested concentration (10 mM) did not yield any FeS_2 NP assemblies because Na^+ and Ca^{2+} cations are not able to form stable complexes with carboxylates; this was also found to be true for coordination polymers (SI). These experiments also demonstrate that salt screening of electrostatic repulsion between NPs facilitating van der Waals attraction and hydrogen bonding between them cannot produce nanosheets by itself without the coordination bonds.

The assembly of FeS_2 NPs induced by $MnCl_2$ and $CuCl_2$ also gave well-defined sheets (Figs S12a-b). Coordination with $RuCl_2$ led to disorganized aggregates (Fig. S12c). One of the potential causes for transition to a different assembly pattern for Ru^{2+} is the high strength of coordination bonds between carboxylates and d^6 metals. One of the potential causes for transition to a different assembly pattern for Ru^{2+} could be the dominance of kinetic factors over thermodynamic under described conditions due to exceptional strength of coordination bonds with d^6 transition metals.

Aqueous dispersion of FeS_2 NPs (FeS_2: 12.0 mg L^{-1}) and $ZnCl_2$ (10 mmol L^{-1}) were mixed at different pH values.

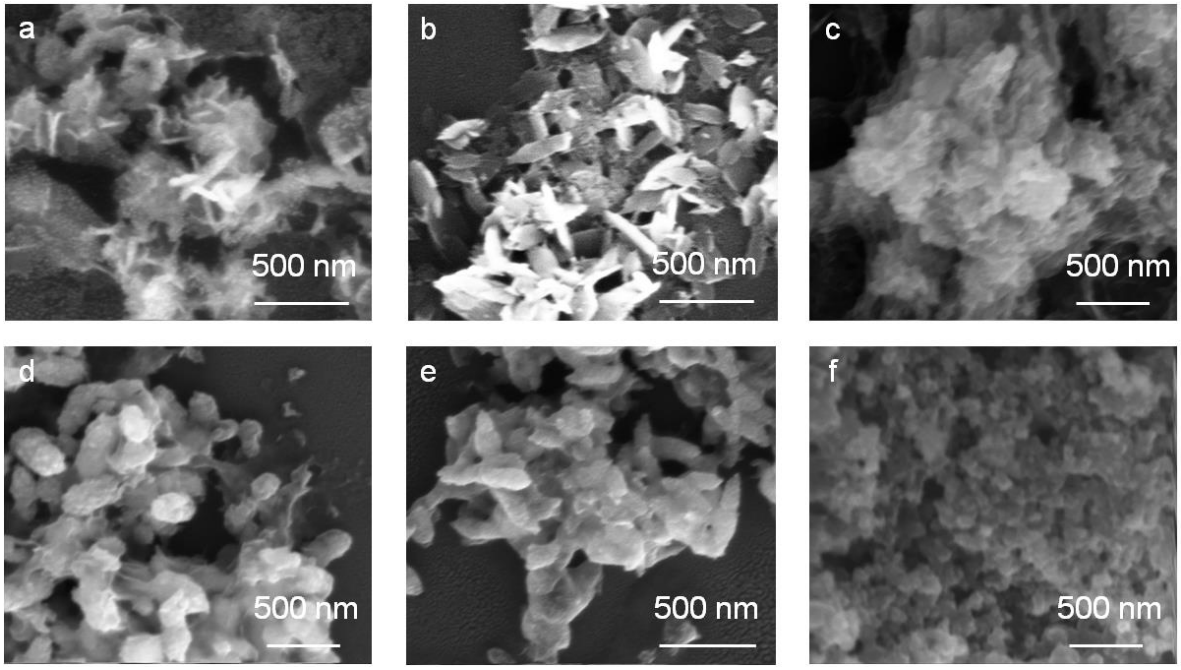

Figure S9. SEM images of the precipitates obtained by mixing $ZnCl_2$ and FeS_2 NPs at (a) pH 5, (b) pH 6, (c) pH 7, (d) pH 8, (e) pH 9 and (f) pH 10.

Comment 5: The pK_a of the free carboxylic acid in TGA is known to be 3.67.[S7] Acidity of the stabilizers is known to change when adsorbed on NPs and depend on the curvature of their surface.[S6]

Aqueous solutions of NPs and $ZnCl_2$ were mixed in different ratios and concentrations and examined after 48 h of incubation. Low concentrations of NPs (FeS_2: 1.2 g mL^{-1}) did not give the sheet form, regardless of the concentration of $ZnCl_2$. A certain amount of $ZnCl_2$ (10 mM) was also required to form the sheets, even when a sufficient amount of NP (12.0 g mL^{-1}) is present in the reaction media. In contrast, excess $ZnCl_2$ (100 mM) led to the merger of several sheets into extended aggregates (Fig. S10a and d, next page).

Table S1. Mixing various concentrations of NPs and $ZnCl_2$.

FeS_2 NPs \ $ZnCl_2$	**100 mmol L^{-1}**	**10 mmol L^{-1}**	**1 mmol L^{-1}**
120 g mL^{-1}	Fig. S8a	Fig. S8b	Fig. S8c
12 g mL^{-1}	Fig. S8d	Fig. S8e	No precipitate
1.2 g mL^{-1}	No precipitate	No precipitate	No precipitate

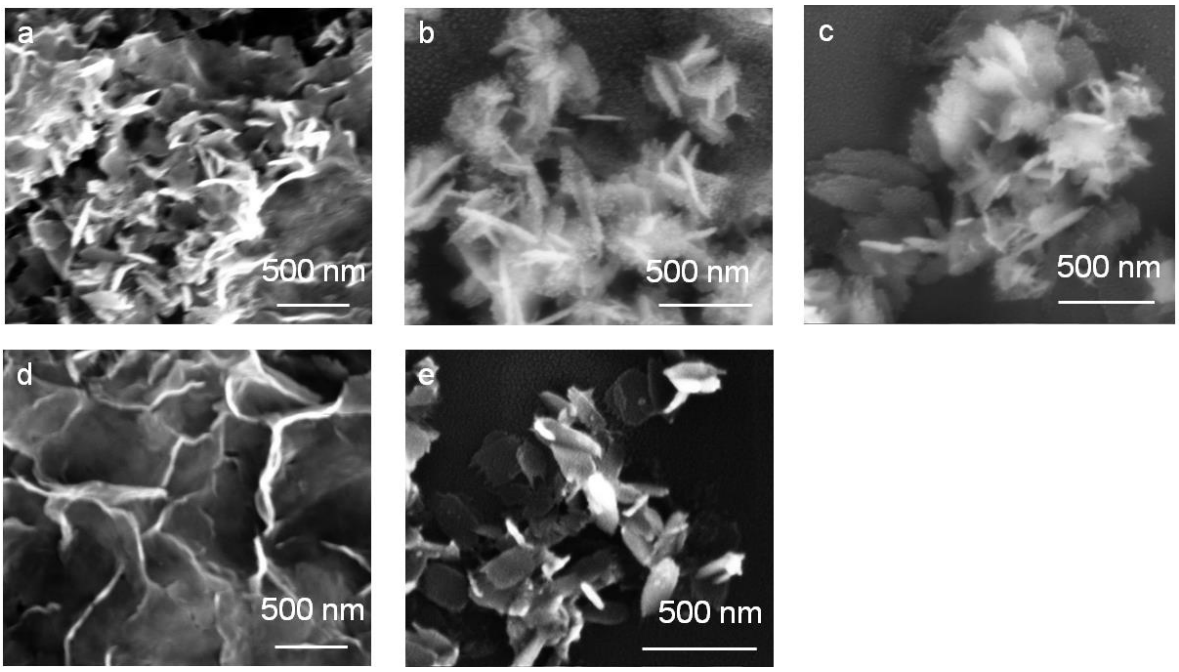

Figure S10. SEM images of precipitates obtained under various conditions listed in Table S1. (a) $ZnCl_2$ (100 mM) and FeS_2 (120 mg L^{-1}), (b) $ZnCl_2$ (10 mM) and FeS_2 (120 mg L^{-1}), (c) $ZnCl_2$ (1 mM) and FeS_2 (120 mg L^{-1}), (d) $ZnCl_2$ (100 mM) and FeS_2 (12.0 mg L^{-1}), (e) $ZnCl_2$ (10 mM) and FeS_2 (12.0 mg L^{-1}).

Aqueous solutions of NPs (12.0 mg L^{-1}) and $ZnCl_2$ (10 mmol L^{-1}) were mixed and examined after 48 h of incubation under different temperatures. When the solutions of NPs and $ZnCl_2$ solutions with appropriate concentrations were mixed (FeS_2: 12 g mL^{-1}, $ZnCl_2$: 10 mM), sheets were obtained between 2 °C and 20°C (Fig. S11a-b). In contrast, mixing $ZnCl_2$ and NPs at 70 °C resulted gave mesoscale rods (Fig. S11c, S1c) with crystallinity different than that in (a,b) (see Fig. S1c).

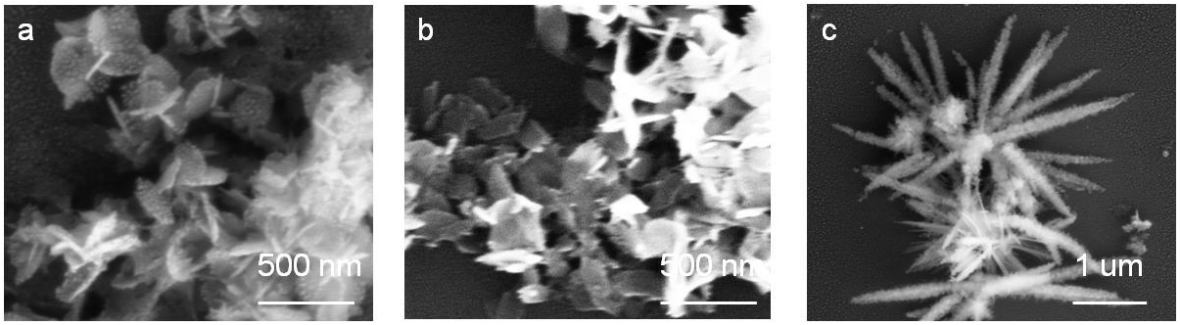

Figure S11. SEM images of the precipitates obtained at different temperatures. The aqueous solutions of NPs (12.0 mg L^{-1}) and $ZnCl_2$ (10 mmol L^{-1}) were mixed at (a) 2 °C, (b) 20 °C and (c) 70 °C.

Aqueous solutions of NPs (12.0 mg L^{-1}) and $CuCl_2$ (10 mmol L^{-1}), $MnCl_2$ (10 mmol L^{-1}) or $RuCl_2$ (10 mmol L^{-1}) were mixed at pH 6 and examined after 48 h of incubation at room temperature.

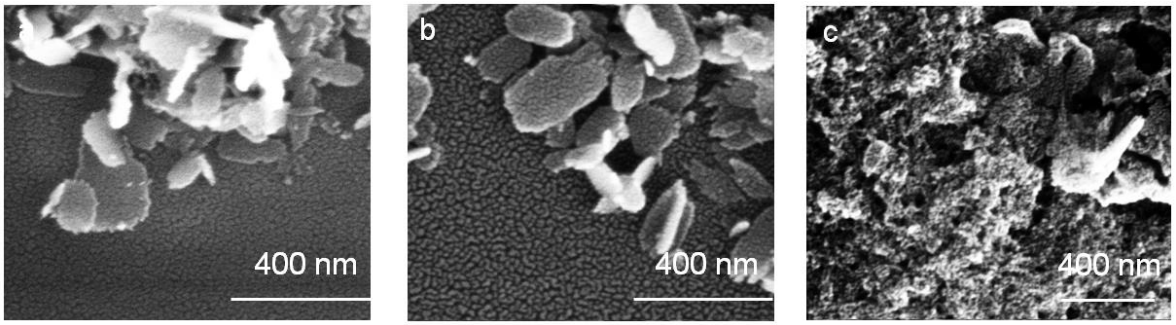

Figure S12. SEM images of the precipitates obtained by mixing 0.5 mL of NP solution (12.0 mg L^{-1}) with 0.5 mL of solution (10 mmol L^{-1}) of (a) $CuCl_2$, (b) $MnCl_2$, (c) $RuCl_2$.

Comment 6: The strength of coordination bonds between carboxylates and alkaline earth metal ions is much weaker than those with post-transition metal ions, such as Zn^{2+}. These differences between metal ion coordinations are well-known from coordination chemistry and studies of coordination polymers.[S8] In contrast, coordination complexes of Ru(II) with carboxylates (and many other groups with lone paired electrons) are typically stronger than those of Zn(II); they also form rapidly. [S9]

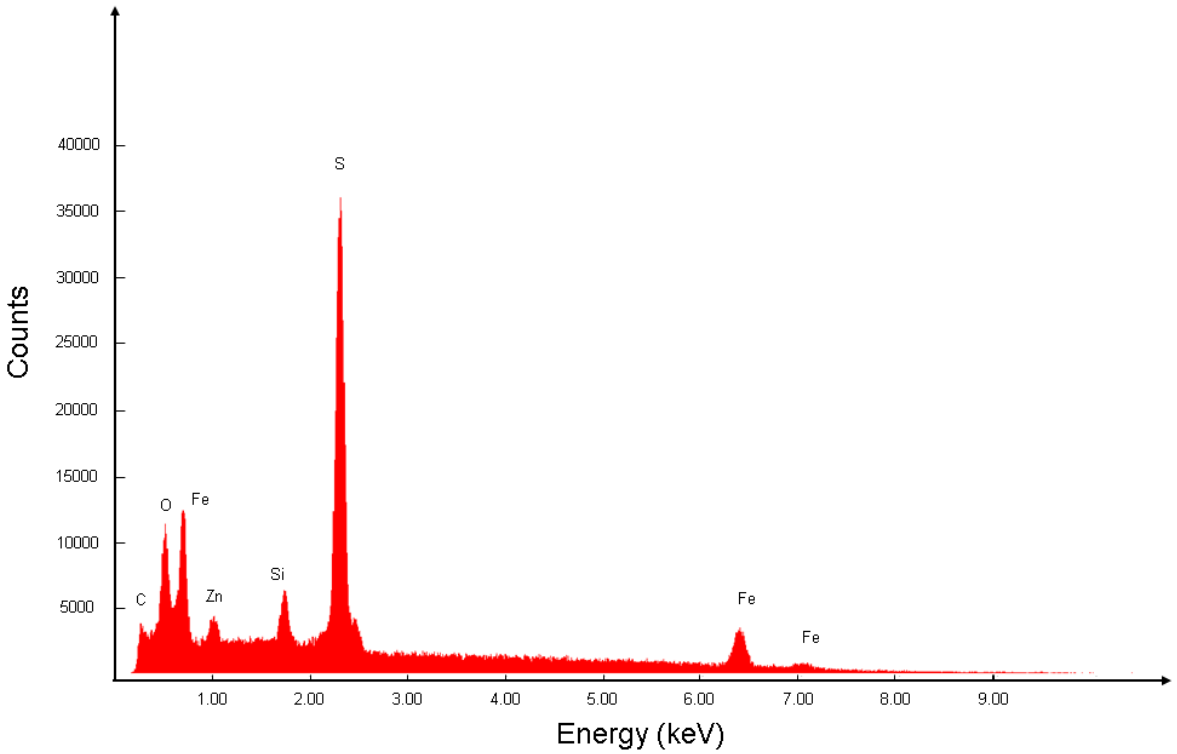

Figure S13. EDX spectrum of the $(NP/Zn^{2+})_{200}$ obtained by the coordination assembly of NPs.

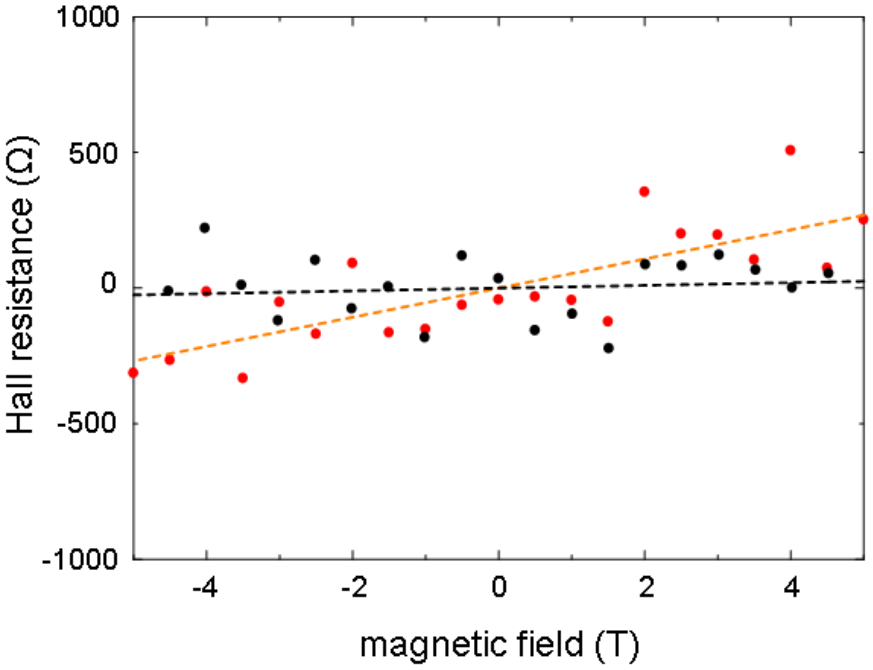

Figure S14. Hall effect measurements of $(NP/Zn^{2+})_{200}$ (red) and drop-cast NPs (black). The orange and black dashed lines indicate the linear fitting for $(NP/Zn^{2+})_{200}$ and drop-cast NP films, respectively.

Table S2. Electrical properties of pyrite and NP-based semiconductor films.

Material	Carrier Type	Conductivity (S/cm)	Carrier Mobility (cm^2/Vs)	Carrier Density (cm^{-3})	Reference
drop-cast NPs*	p	0.0661 (10K) 0.0728 (RT)	2.06	1.99×10^{17}	this work
$(NP/Zn^{2+})_{200}$*	**p**	**0.668 (10K)** **0.716 (RT)**	**19.0**	**2.19×10^{17}**	**this work**
single crystalline pyrite (chemical vapor deposition)	p	7.1 (RT)	0.42	2.1×10^{18}	S10
polycrystalline pyrite (flux growth)	n	1.25 (RT)	366	2.1×10^{16}	S11
Co-doped pyrite film (chemical vapor deposition)	n	-	1.5	10^{20}	S12
pyrite film (sol-gel)	p	-	1.5	10^{19}	S13
pyrite NP film (solution-phase deposition)	p	0.526 (RT)	1 >	-	S14
CdSe NP film (spin coating)	n	10^{-3}	0.01	-	S15
CdSe NP film (evaporative assembly with organometalic bridges)	n	-	0.03	-	S16
PbTe/Ag_2Te	p	0.346 (RT)	-	-	S17

* The Hall measurements in this work were carried out at 10 K. Hall coefficient (R_H), carrier mobility (μ_h) and density (n_h) are calculated by following the equations.

$\mu_h = R_H \times \sigma$, $n_h = 1/(R_H \times e)$, R_H = (Hall Resistance × thickness)/Magnetic Field

Table S3. Conductivity of coordination polymers.

Coordination Polymer	**Conductivity (S cm^{-1})**	**Reference**
$Cu[Cu(pdt)_2]$ pdt = 2,3-pyrazinedithiolate	6×10^{-4}	S18
$Ni[Cu(pdt)_2]$	1×10^{-8}	S19
$[Fe(ptt)]_n(H_2O)_m$ Ptt = phenyl-1,2,4,5-tetrathiolate	0.2	S20
$[Ni(ptt)]_n(H_2O)_m$	2×10^{-3}	S20
$Co_2(ptt)_{11}$	2×10^{-3}	S20
[Cu(ptt)]	2×10^{-5}	S20

Comment 7: These publications do not report carrier signs and values of carrier mobility and carrier density. The reason is likely to be the difficulty with Hall measurements due to low conductivity.

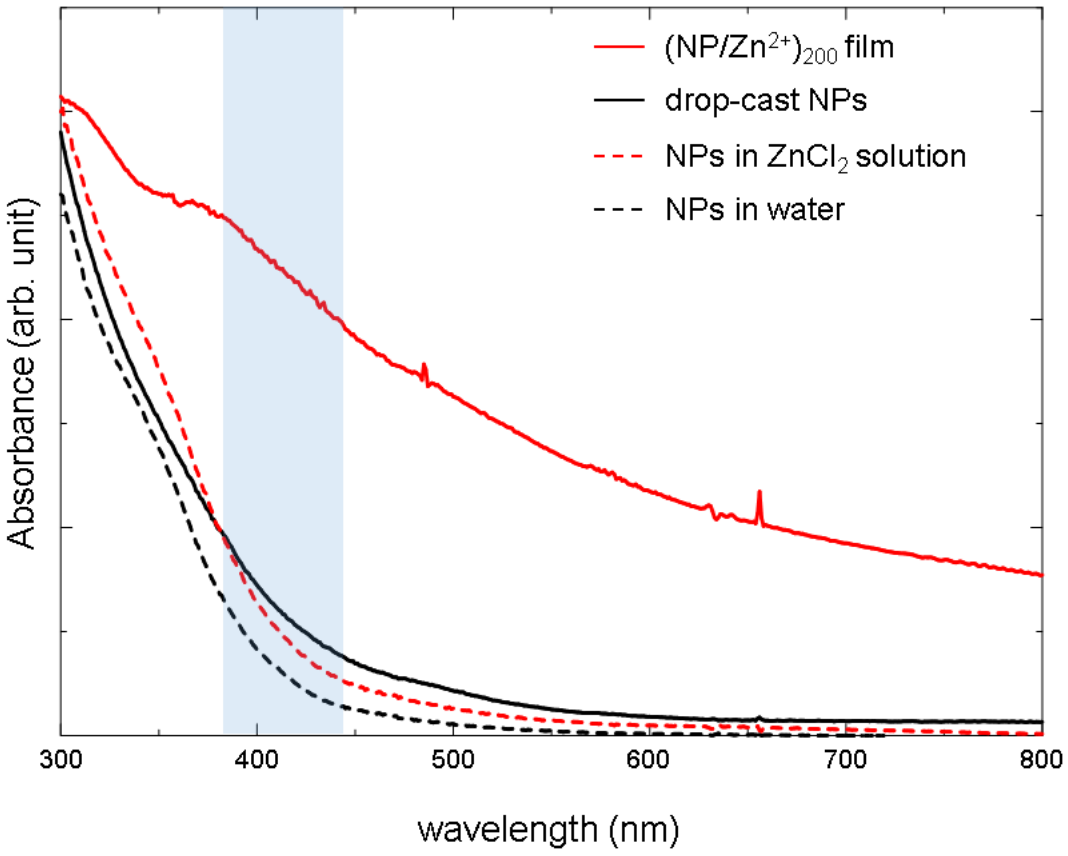

Figure S15. UV spectra of the $(NP/Zn^{2+})_{200}$, drop-cast NP films, NPs in $ZnCl_2$ aqueous solution and NPs in water. The blue region is the spectral window used for photocurrent measurements in Fig. S16.

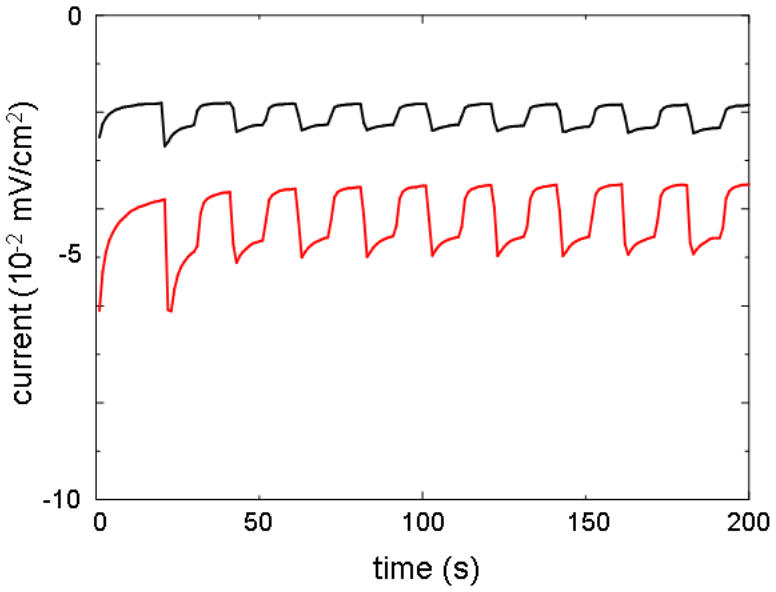

Figure S16. Photocurrent response of $(NP/Zn^{2+})_{200}$ (red) and drop-cast NPs (black). The light was switched on and off every 10 seconds.

Comment 8: $(NP/Zn^{2+})_{200}$ and drop-cast NP films displayed an increase of reduction current in response to the illumination with light with λ = 380-440 nm (120 W lamp, applied potential: –0.2V). The photocurrent density for $(NP/Zn^{2+})_{200}$ was 1.8×10^{-2} mA cm^{-3}. It was considerably higher than photocurrent density for drop-cast NP films 9.0×10^{-3} mA cm^{-3}. However, the increase of the photocurrent for $(NP/Zn^{2+})_{200}$ is associated with contributions of several factors; of which improvement of charge transport between NPs is one of the factors. As seen in the result of Hall Effect measurements, $(NP/Zn^{2+})_{200}$ showed the high electronic conductivity because of the facile charge transport via coordination bridging of NPs. The efficient charge transport between NPs can also contribute to the higher photocurrent. More efficient light absorption at 390 nm $(NP/Zn^{2+})_{200}$ (Fig. S15) represents another significant factor that is definitely at play here.

Table S4. Electrochemical reduction of benzyl chloride.

	Potential vs Ag/AgCl E_r (V)	**Concentration of benzyl chloride**	**Solution**	**Citation**
(NP/Zn^{2+})$_{200}$ film	**–1.13 (Light)** **–1.20 (Dark)**	**10 mM**	**0.05 M Et_4NBF_4 (CH_3CN)**	**this work**
Drop-cast NPs	–1.25 (Light) –1.32 (Dark)	10 mM	0.05 M Et_4NBF_4 (CH_3CN)	this work
graphite	–1.4	0.2 mmol*	0.1 M KBr (water)	S21
1.48 mM Co(salen)	–1.17	15.43 mM	0.1 M Bu_4NClO_4 (CH_3CN)	S22
Ag/Pd NP	–1.26	10 mM	0.05 M Et_4NBF_4 (CH_3CN)	S23
Ag NP	–1.82	10 mM	0.05 M Et_4NBF_4 (CH_3CN)	S24
Ag/Au NP	–1.64	10 mM	0.05 M Et_4NBF_4 (CH_3CN)	S24

* benzyl chloride was impregnated in graphite

Supplementary References.

[S1]. Y. Bai, J. Yeom, M. Yang, S. Cha, K. Sun, N. A. Kotov, *J. Phys. Chem. C* **2013**, *117*, 2567-2573.

[S2]. E. Biemmi, C. Scherb, T. Bein, *J. Am. Chem. Soc.* **2007**, *129*, 8054-8055.

[S3]. S. Hermes, F. Schröder, R. Chelmowski, C. Wöll, R. A. Fischer, *J. Am. Chem. Soc.* **2005**, *127*, 13744-13745.

[S4]. D. Prochowicza, K. Sokołowski, J. Lewiński, *Coord. Chem. Rev.* **2014**, *270-271*, 112-126.

[S5]. M. Eddaoudi, J. Kim, N. Rosi, D. Vodak, J. Wachter, M. O'Keeffe, O. M. Yaghi, *Science* **2012**, *295*, 469-472.

[S6]. D. Wang, R. J. Nap, I. Lagzi, B. Kowalczyk, S. Han, B. A. Grzybowski, I. Szleifer, *J. Am. Chem. Soc.* **2011**, *133*, 2192-2197.

[S7]. J. T. Edsall, J. Wyman, *Biophys. Chem. Acad. Press,* Inc., New York, 1958

[S8]. N. S. Poonia, A. V. Bajaj, *Chem. Rev.* **1979**, *79*, 389-445.

[S9]. H. Taube, *Chem. Rev.* **1952**, *50*, 69-126.

[S10]. O. Blenk, E. Bucher, G. Willeke, *Appl. Phys. Lett.* **1993**, *62*, 2093-2095.

[S11]. R. Schieck, A. Hartmann, S. Fiechter, R. Könenkamp, H. Wetzel, *J. Mater. Res.* **1990**, *5*, 1567-1572.

[S12]. B. Thomas, K. Ellmer, W. Bohne, J. Röhrich, M. Kunst, H. Tributsch, *Solid State Commun.* **1999**, *111*, 235-240.

[S13]. L. Huang, F. Wang, Z. Luan, L. Meng *Mater. Lett.* **2010**, *64*, 2612-2615.

[S14]. S. Seefeld *et al.*, *J. Am. Chem. Soc.* **2013**, *135*, 4412-4424.

[S15]. D. Yu, B. L. Wehrenberg, P. Jha, J. Ma, P. Guyot-Sionnest, *J. Appl. Phys.* **2006**, *99*, 104315-104317.

[S16]. M. V. Kovalenko, M. Scheele, D. V. Talapin, *Science* **2009**, *324*, 1417-1420.

[S17]. J. J. Urban, D. V. Talapin, E. V. Shevchenko, C. R. Kagan, C. B. Murray, *Nature Mater.* **2007**, *6*, 115-121.

[S18]. S. Takaishi *et al.*, *Inorg. Chem.* **2009**, *48*, 9048-9050.

[S19]. Y. Kobayashi, B. Jacobs, M. D. Allendorf, J. R. Long, *Chem. Mater.* **2010**, *22*, 4120-4122.

[S20]. C. W. Dirk, M. Bousseau, P. H., Barrett, F. Moraes, F. Wudl, A. J. Heeger, *Macromolecules* **1986**, *19*, 266-269.

[S21]. R. F. M. de Souza *et al. Electrochimica Acta* **2010**, *56*, 575-579.

[S22]. A. A. Isse, A. Gennaro, E. Vianello, *J. Electroanal. Chem.* **1998**, *444*, 241-245.

[S23]. C. An, Y. Kuang, C. Fu, F. Zeng, W. Wang, H. Zhou, *Electrochem. Commun.* **2011**, *13*, 1413-1416.

[S24]. G. Zhang, Y. Kuang, J. Liu, Y. Cui, J. Chen, H. Zhou, *Electrochem. Commun.* **2010**, *12*, 1233-1236.